Theor Chem Acc (2007) 117:383–395
DOI 10.1007/s00214-006-0166-5

REGULAR ARTICLE

Hybrid density functional theory with a specific reaction parameter: hydrogen abstraction reaction of trifluoromethane by the hydroxyl radical

Titus V. Albu · Saravanan Swaminathan

Received: 25 May 2006 / Accepted: 28 July 2006 / Published online: 26 September 2006

Abstract Potential energy surfaces are developed and tested for the $OH + CHF_3 \rightarrow H_2O + CF_3$ reaction. The objective is to obtain surfaces that give calculated rate constants comparable to the experimental ones. The potential energy surfaces are constructed using hybrid and hybrid meta density functional theory methods (mPW1PW91, B1B95, and mPW1B95) with specific reaction parameters in conjunction with the 6–31+G(d,p) basis set. The rate constants are calculated over the temperature range 200–1,500 K using variational transition state theory with multidimensional tunneling contributions. The hybrid density functional theory methods with specific-reaction-parameter Hartree-Fock exchange contributions (32.8–34.8% for mPW1PW91, 34.2–36.0% for B1B95, and 37.8–39.7% for mPW1B95, respectively) provide accurate rate constants over an extended temperature range. The classical barrier height for the hydrogen abstraction reaction is determined to be 6.5–6.9 kcal/mol on these potential energy surfaces, and the best estimate value is 6.77 kcal/mol.

Keywords Hydrogen abstraction · Trifluoromethane · Barrier height · Rate constant

Electronic supplementary material The online version of this article (doi:10.1007/s00214-006-0166-5) contains supplementary material, which is available to authorized users.

T. V. Albu (✉) · S. Swaminathan
Department of Chemistry,
Tennessee Technological University,
P.O. Box 5055, Cookeville, TN 38505, USA
e-mail: albu@tntech.edu

1 Introduction

Chlorofluorocarbons are the major source of stratospheric chlorine, which could become active chlorine and destroy ozone in the stratosphere [1,2]. Industry has developed two classes of halocarbon substitutes: hydrochlorofluorocarbons (HCFCs) and hydrofluorocarbons (HFCs). However, the HCFCs still contain chlorine and can potentially destroy the ozone. Therefore, the chlorine-free compounds are considered better substitutes for chlorofluorocarbons. The HFCs have a wide range of applications in refrigeration, polyurethane foam production, fire suppressants, rocket fuels, etc. The HFC under consideration in this work is trifluoromethane, industrially known as R23.

The attack by a hydroxyl radical on the C–H bonds in HFCs are important atmospheric reactions, and, in this work, we investigate the reaction of hydroxyl radical with trifluoromethane molecule resulting in the hydrogen abstraction and the formation of water:

$$OH + CHF_3 \rightarrow H_2O + CF_3 \quad (1)$$

The rate constant of this reaction has been experimentally determined in a number of studies [3–8]. In the current investigation, we consider four Arrhenius experimental fits:

$$k = 6.93 \times 10^{-13} \exp(-2,300/T) \text{cm}^3 \text{ molecule}^{-1} \text{ s}^{-1} \quad (2)$$

$$k = 6.4 \times 10^{-13} \exp(-2,354/T) \text{cm}^3 \text{ molecule}^{-1} \text{ s}^{-1} \quad (3)$$

$$k = 3.02 \times 10^{-12} \exp(-2,910/T) \text{cm}^3 \text{ molecule}^{-1} \text{ s}^{-1} \quad (4)$$

$$k = 1.1 \times 10^{-12} \exp(-2,300/T) \text{cm}^3 \text{ molecule}^{-1} \text{ s}^{-1} \quad (5)$$

proposed by Schmoltner et al. [6] for the temperature range 232–378 K, by Hsu and DeMore [7] for the

temperature range 298–383 K, by Jeong and Kaufman [5] for the temperature range 387–480 K, and by Medhurst et al. [8] for the temperature range 500–750 K, respectively.

A large number of theoretical studies have focused on the dynamics of this reaction [9–16]. Louis et al. [14] calculated the rate constants by means of conventional transition state theory (TST) using the MP2/6-311G(2d,2p) electronic structure method [17] with single-point corrections at PMP4(SDTQ) level of theory [18–20] and tunneling contributions calculated with the Wigner formula [21]. Korchowiec et al. [13] also calculated the rate constants; they used modified G2 [22–24] electronic structure theory and conventional TST with the Wigner formula for tunneling contributions. The modified G2 [24] value of the classical barrier height was determined to be 5.8 kcal/mol. The studies of Schwartz et al. [12] and Fu et al. [11] also employed the TST calculations of the rate constants but with tunneling contributions calculated for one-dimensional Eckart barriers [25].

In the present study, variational transition state theory with multidimensional tunneling contributions (VTST/MT) [26–36] is used to calculate the rate constants for the title reaction. The VTST/MT is a powerful and affordable method for studying chemical reaction dynamics, and its accuracy is primarily limited by the level of electronic structure theory used for the potential energy surface (PES) underlying the dynamics. The hybrid density functional theory (HDFT) is an excellent candidate for generating an accurate PES because it is an easily parameterized and affordable electronic structure method. The hybrid density functionals have been shown to accurately predict a wide variety of molecular and dynamics properties such as molecular geometries, atomization energies, barrier heights, intermolecular interactions, etc. [37–40]. The procedure used here involves generating the hybrid density functionals that provide accurate rate constants in conjunction with direct dynamics calculations using the VTST/MT. We developed the hybrid density functionals with a specific reaction parameter (SRP) [41] for the $HO + CH_3F$ reaction [42], and in the present study we extend this approach to the $HO + CHF_3$. (A similar approach was applied by Pu and Truhlar [43] for constructing a PES for the $H + CH_4 \rightarrow H_2 + CH_3$ reaction.) Three new HDFT-SRP methods (with one parameter each) that provide accurate rate constants over a wide temperature range are proposed. The advantage of these accurate PESs is that the rate constants are obtained on a single-level PES rather than using dual-level dynamics techniques. (Dual-level dynamics methods [44–47] are typically used because the dynamics calculations using only the higher level of theory are computationally prohibited, and those using only the lower level of theory are not reliable.) The approach used here allows for a good description of the stationary point geometry and a more advanced, multidimensional treatment of the tunneling contributions to the calculated rate constants. The procedure is extendable to other hydrogen abstraction reactions from the HFCs or other classes of reactions.

Section 2 provides an overview of the theory and the computational methodology used, Sect. 3 presents the results, and Sect. 4 gives analyses and discussions. Conclusions and future applications are provided in the final section.

2 Computational methodologies

2.1 Variational transition state theory with multidimensional tunneling contributions

The rate constants are calculated using the variational transition state theory with the multidimensional tunneling contributions [26–36]. The transition state can be understood classically as a dividing surface (also called a generalized transition state) in phase space; it divides the space into a reactant region and a product region [33,35]. In variational transition state theory, the position of the dividing surface is optimized so that trajectories originating at reactants and passing through the dividing surface toward the product region will not recross the surface before being thermalized in the product state. The canonical variational-transition-state theory (CVT) rate constant, k^{CVT}, is obtained by maximizing the generalized free energy of activation (at temperature T), ΔG_T^{GT}, as a function of the position of the generalized transition state along the reaction path. The reaction path is the minimum energy path (MEP) that is defined as the steepest descent path from the saddle point to both the reactant and the product sides in the mass weighted (isoinertial) Cartesian coordinate system in which all coordinates are scaled to a common reduced mass μ [48]. The reaction coordinate, s, is defined as the distance along the MEP with the origin located at the saddle point and is positive on the product side and negative on the reactant side. The maximum in ΔG_T^{GT} determines the location along the MEP of the dynamical bottleneck at a certain temperature, $s_*^{\mathrm{CVT}}(T)$. The CVT free energy of activation is obtained as:

$$\Delta G_T^{\mathrm{CVT}} = \max_s \Delta G_T^{\mathrm{GT}}(s) \tag{6}$$

and k^{CVT} is given by:

$$k^{CVT}(T) = \sigma \frac{k_B T}{h} \exp(-\Delta G_T^{CVT}/RT) \quad (7)$$

where k_B is Boltzmann's constant, h is Planck's constant, and R is the gas constant. The symmetry factor, σ, calculated as the ratio of the product of the reactant rotational symmetry numbers to that of the transition state [49], is equal to 3 for this reaction. At the saddle point ($s = 0$) one obtains the conventional TST rate constant, k^{TST}, and the saddle point free energy of activation $\Delta G_T^{\ddagger}$. Any deviation of k^{CVT} from k^{TST} is called a variational effect. Calculation of the generalized free energy of activation involves calculation of partition functions that are approximated as products of translational, rotational, vibrational, and electronic partition functions. The translational and rotational partition functions were classically evaluated without symmetry numbers whereas the vibrational partition functions were calculated quantum mechanically within the harmonic approximation. Although anharmonicity is known to be important [28,50,51], one can assume a certain amount of cancellation between the anharmonic corrections for the reactant and for the generalized transition states [28].

Quantum mechanical effects along the reaction coordinate are included in this study in the form of temperature-dependent transmission coefficients, κ, that primarily account for multidimensional tunneling. The rate constants including tunneling contributions are computed as:

$$k^{CVT/MT}(T) = \kappa^{MT}(T) k^{CVT}(T) \quad (8)$$

where κ^{MT} is the transmission coefficient. The tunneling calculation is based in part on $V_a^G(s)$, which is the vibrationally adiabatic ground-state potential energy curve defined, for nonlinear systems, as:

$$V_a^G(s) = V_{MEP}(s) + \sum_{m=1}^{3N_{atoms}-7} \frac{\hbar \omega_m(s)}{2} \quad (9)$$

where V_{MEP}(s) is the classical potential energy along the MEP (with its zero of energy at the reactants), $\omega_m(s)$ is the frequency of generalized normal mode m at location s along the MEP, and N_{atoms} is the total number of atoms in the reactive system (seven for the title reaction). In the present study, the multidimensional transmission coefficients were computed using the centrifugal-dominant, small-curvature, semiclassical, adiabatic, ground-state tunneling (called small-curvature tunneling or SCT) approximation [34,52], version 4 of the large-curvature tunneling (LCT) approximation [53–56], and the microcanonical optimized multidimensional tunneling (μOMT) approximation [53,55]. The LCT results include tunneling into vibrationally excited states. The μOMT results are obtained by selecting, for any total energy, the larger of the SCT and LCT probabilities. Calculations using the one-dimensional zero-curvature tunneling (ZCT) approximation were also carried out.

2.2 Hybrid density functional theory methods

The electronic structure theory methods for all calculations in this study are HDFT methods. In an HDFT method, the one-parameter hybrid Fock–Kohn–Sham operator can be written as:

$$F = F^H + XF^{HFE} + (1 - X)(F^{SE} + F^{GCE}) + F^C \quad (10)$$

where F^H is the Hartree operator (i.e., the nonexchange part of the Hartree–Fock operator), F^{HFE} is the Hartree–Fock exchange operator, X is the fraction of Hartree–Fock (HF) exchange, F^{SE} is the Dirac–Slater local density functional for exchange, F^{GCE} is the gradient correction for the exchange functional, and F^C is the total correlation functional including both local and gradient-corrected parts. The functionals used here are mPW1PW91 [57–59], B1B95 [60–63], and mPW1B95 [38,58,62] in conjunction with the 6–31+G(d,p) basis set. We will refer in the rest of the paper to all methods as just HDFT methods even though, to be precise, whereas mPW1PW91 is a hybrid DFT, mPW1B95 and B1B95 are actually hybrid meta DFT methods.

In the SRP approach employed here, we parameterized the value of X in Eq. (10) to create potential energy surfaces that yield the VTST/MT rate constants very close to the experimental ones. The HDFT methods obtained for different values of X are labeled by defining the gradient correlated exchange functional used, followed by 1 to indicate a one-parameter method, followed by the correlation functional used, and finally by the value of X (given as a percent) separated by a dash. For example, mPW1PW91–33.5 represents a hybrid density functional theory method based on modified Perdew–Wang (mPW) [58] gradient-corrected exchange functional and PW91 [57] gradient-corrected correlation functional with 33.5% HF exchange contribution. The K methods (MPW1K, BB1K, and MPWB1K) developed by Truhlar and co-workers [38,59,63] were relabeled according to the earlier convention as mPW1PW91—42.8, B1B95—42.0, and mPW1B95—44.0, respectively.

2.3 Computational details

All electronic structure calculations were carried out using *Gaussian*03 software [64]. The geometry optimizations were performed using a tight convergence criteria and an ultrafine integration grid for numerical integrations. Restricted wave functions were used for closed-shell systems and unrestricted wave functions for open-shell systems.

Direct dynamics calculations are carried out with the GAUSSRATE [65] computer program, which interfaces the POLYRATE [66] and GAUSSIAN [64] programs. The partition functions were calculated assuming the rigid rotor-harmonic oscillator approximation. In calculating the electronic partition function of the hydroxyl radical, we included the $^2\Pi_{1/2}$ electronic excited state with excitation energy of 140 cm^{-1} . For the generalized transition state, no low-lying electronically excited states were considered so the electronic partition function was the ground state multiplicity, which is 2. The MEP in isoinertial coordinates was calculated by the Page–McIver method [67]. In all direct dynamics calculations, the coordinates were scaled to a reduced mass μ of 1 amu. A step size of 0.005 a_0 between gradient calculations was used, and a Hessian was calculated every 0.05 a_0 along the MEP. Calculations were carried out far enough along the reaction path to fully converge the tunneling calculations. The vibrational frequencies along the reaction path were evaluated using a set of redundant internal coordinates [68] that consists of 6 stretches, 11 nondegenerate bends, and 3 torsions. The choice of these redundant internal coordinates that were used in generalized, normal-mode, vibrational analyses, yielded in each case a reaction-path Hamiltonian with all frequencies real along MEP in the region relevant to the kinetics.

3 Results

The results of our calculations are presented in five tables and six figures. In Table 1, the energetic parameters for reaction 1 calculated with different HDFT methods are presented. In this table, ΔE is the classical energy of reaction, ΔH_0 is the zero-point-inclusive energy of reaction, $V^{\ddagger}$ is the classical (i.e., zero-point-exclusive) barrier height, $\Delta H_0^{\ddagger}$ is the zero-point-inclusive barrier height, $E_a^{\ddagger}$ is Arrhenius activation energy at 298 K obtained on the basis of k^{TST}, $E_a^{V/T}$ is Arrhenius activation energy at 298 K obtained on the basis on $k^{CVT/SCT}$, $\Delta G_{298}^{\ddagger}$ is the conventional TST free energy of activation at 298 K, and $\omega^{\ddagger}$ is the imaginary frequency at the saddle point. The zero-point-inclusive barrier height, $\Delta H_0^{\ddagger}$, is calculated as:

Table 1 Energetic parameters for $OH + CHF_3 \rightarrow H_2O + CF_3$ reaction

HDFT method	ΔE	ΔH_0	$V^{\ddagger}$	$\Delta H_0^{\ddagger}$	$E_a^{\ddagger}$	$E_a^{V/T}$	$\Delta G_{298}^{\ddagger}$	$\omega^{\ddagger}$
mPW1PW91– *X*/6–31+G(d,p)								
$X = 25.0$	−10.9	−11.1	4.1	1.9	2.4	NC[a]	7.6	1146 *i*
$X = 30.7$	−10.1	−10.2	5.8	3.5	4.0	4.7	9.2	1423 *i*
$X = 33.5$	−9.7	−9.8	6.6	4.3	4.9	5.2	10.1	1534 *i*
$X = 35.7$	−9.3	−9.5	7.3	4.9	5.5	5.7	10.7	1613 *i*
$X = 42.8$[b]	−8.3	−8.5	9.3	6.9	7.5	7.1	12.7	1837 *i*
B1B95– *X*/6–31+G(d,p)								
$X = 28.0$	−11.3	−11.4	4.6	2.4	2.9	NC	8.1	1151 *i*
$X = 32.1$	−10.6	−10.8	5.8	3.5	4.1	4.8	9.2	1352 *i*
$X = 34.8$	−10.2	−10.4	6.6	4.3	4.8	5.3	10.0	1465 *i*
$X = 37.0$	−9.9	−10.0	7.2	4.9	5.4	5.8	10.6	1547 *i*
$X = 42.0$[c]	−9.1	−9.3	8.6	6.2	6.8	6.7	12.0	1715 *i*
mPW1B95– *X*/6–31+G(d,p)								
$X = 31.0$	−11.0	−11.1	4.5	2.2	2.8	NC	7.9	1268 *i*
$X = 35.4$	−10.3	−10.4	5.8	3.5	4.1	4.6	9.2	1463 *i*
$X = 38.5$	−9.8	−9.9	6.7	4.4	5.0	5.2	10.1	1579 *i*
$X = 41.0$	−9.4	−9.5	7.5	5.1	5.7	5.7	10.8	1665 *i*
$X = 44.0$[d]	−8.9	−9.1	8.3	6.0	6.5	6.3	11.7	1760 *i*

All values are in kcal/mol except the imaginary frequency that is in cm^{-1}

[a] n.c. denotes not calculated

[b] MPW1K

[c] BB1K

[d] MPWB1K

Table 2 Geometric parameters for the saddle point of $OH + CHF_3 \rightarrow H_2O + CF_3$ reaction

HDFT method	$r^{\ddagger}_{C\cdots H}$	$r^{\ddagger}_{H\cdots O}$	$r^{\ddagger}_{C\cdots O}$	$\theta^{\ddagger}_{C\cdots H\cdots O}$
mPW1PW91– *X*/6–31+G(d,p)				
$X = 25.0$	1.224	1.280	2.498	172.5
$X = 30.7$	1.235	1.256	2.485	172.4
$X = 33.5$	1.239	1.246	2.479	172.3
$X = 35.7$	1.242	1.240	2.476	172.3
$X = 42.8$	1.250	1.221	2.465	172.1
B1B95– *X*/6–31+G(d,p)				
$X = 28.0$	1.223	1.283	2.501	172.6
$X = 32.1$	1.231	1.265	2.491	172.5
$X = 34.8$	1.235	1.255	2.485	172.4
$X = 37.0$	1.238	1.248	2.480	172.4
$X = 42.0$	1.244	1.234	2.472	172.2
mPW1B95–X/6–31+G(d,p)				
$X = 31.0$	1.226	1.271	2.492	172.1
$X = 35.4$	1.234	1.254	2.482	172.1
$X = 38.5$	1.238	1.244	2.476	172.0
$X = 41.0$	1.241	1.237	2.472	171.9
$X = 44.0$	1.245	1.229	2.467	171.8

All distances are in A, the angles are in degrees

$$\Delta H_0^{\ddagger} = V^{\ddagger} + \sum_{m=1}^{14} \frac{\hbar\omega_m^{\ddagger}}{2} - \sum_{n=1}^{9} \frac{\hbar\omega_n^{CHF_3}}{2} - \frac{\hbar\omega^{OH}}{2} \tag{11}$$

where $\omega_m^{\ddagger}$ is the frequency of the normal mode m of the saddle point, $\omega_n^{CHF_3}$ is the frequency of the normal mode n of CHF_3, and ω^{OH} is the hydroxyl normal mode frequency. The Arrhenius activation energies at 298 K, $E_a^{\ddagger}$ and $E_a^{V/T}$, are obtained by fitting k^{TST} and $k^{CVT/SCT}$ to an Arrhenius expression and are calculated as:

$$E_a^{\ddagger} = \frac{RT_1T_2}{T_2 - T_1} \ln \frac{k^{TST}(T_2)}{k^{TST}(T_1)} \tag{12}$$

and

$$E_a^{V/T} = \frac{RT_1T_2}{T_2 - T_1} \ln \frac{k^{CVT/SCT}(T_2)}{k^{CVT/SCT}(T_1)} \tag{13}$$

where $T_1 = 293$ K and $T_2 = 303$ K. In Table 2, selected geometric parameters of the saddle points calculated on different HDFT surfaces are presented.

The calculated rate constants as well as experimental ones (where available) in the temperature range 200–1,500 K are presented in Tables 3, 4, and 5, for mPW1PW91—*X*, B1B95—*X*, and mPW1B95—X functionals, respectively. Only $k^{CVT/SCT}$ are shown in this table; some other calculated rate constants are given as Supplementary Material. The accuracy of the calculated rate constants using various HDFT methods was monitored by means of two statistical measures of the average deviation [55]. The mean unsigned percentage error (MUPE), defined as

$$\text{MUPE} = \left(\frac{1}{N} \sum_{i=1}^{N} \left| \frac{k_i^{calc} - k_i^{exp}}{k_i^{exp}} \right| \right) \times 100\% \tag{14}$$

and the logarithmically averaged percentage error (LAPE) defined as

$$\text{LAPE} = (10^{\text{AUPD}} - 1) \times 100\% \tag{15}$$

$$\text{AUPD} = \frac{1}{N} \sum_{i=1}^{N} \left| \log_{10} \frac{k_i^{calc}}{k_i^{exp}} \right| \tag{16}$$

were used. In these equations, k_i^{calc} represents the calculated rate constant at a certain temperature, k_i^{exp} represents the calculated rate constant at the same temperature, and N is the number of different temperature over which the comparison is made. The MUPE is very familiar and used more extensively but it does not give a balanced representation of the cases in which the calculated rate constants are underestimated that for which the percent error is limited to 100%. The LAPE, however, evenly treats underestimates and overestimates of the experimental rate constants and was used for the analysis of our results. The MUPE and LUPE are also given in Tables 3, 4, and 5.

Figure 1 shows V_{MEP} and V_a^G along the reaction coordinate determined with the mPW1PW91—33.5, B1B95—34.8, and mPW1B95—38.5 functionals, respectively, and the 6–31+G(d,p) basis set [69]. In these figures, all reported energies are relative to the zero-point-exclusive energy of the reactants, which is considered the zero of energy. Figure 2 exhibits a two-dimensional representation of the MEPs calculated at the same levels of theory as Fig. 1, and insets for the saddle point and

Table 3 Calculated ($k^{CVT/SCT}$) and experimental rate constants (in cm^3 $molecule^{-1}$ s^{-1}) determined on various mPW1PW91– *X*/6–31+G(d,p) surfaces as well as the average errors

Temperature (K)	mPW1PW91– *X*/6–31+G(d,p)				Experimental
	$X = 30.7$	$X = 33.5$	$X = 35.7$	$X = 42.8$	
200	2.1(–17)[a]	4.5(–18)	1.4(–18)	3.4(–20)	NA[b]
250	1.8(–16)	4.8(–17)	1.8(–17)	8.3(–19)	7.0(–17)
298	7.7(–16)	2.5(–16)	1.1(–16)	7.7(–18)	2.7(–16)
300	8.1(–16)	2.7(–16)	1.1(–16)	8.4(–18)	2.9(–16)
350	2.6(–15)	9.7(–16)	4.6(–16)	4.8(–17)	8.7(–16)
400	6.4(–15)	2.7(–15)	1.4(–15)	1.9(–16)	2.1(–15)
450	1.4(–14)	6.2(–15)	3.4(–15)	5.6(–16)	4.7(–15)
500	2.6(–14)	1.2(–14)	7.2(–15)	1.4(–15)	1.1(–14)
600	7.0(–14)	3.8(–14)	2.4(–14)	5.8(–15)	2.4(–14)
700	1.5(–13)	8.9(–14)	5.9(–14)	1.8(–14)	4.1(–14)
800	2.9(–13)	1.8(–13)	1.2(–13)	4.2(–14)	NA
900	4.9(–13)	3.2(–13)	2.3(–13)	8.6(–14)	NA
1,000	7.8(–13)	5.2(–13)	3.9(–13)	1.6(–13)	NA
1,200	1.7(–12)	1.2(–12)	9.0(–13)	4.2(–13)	NA
1,500	3.9(–12)	3.0(–12)	2.4(–12)	1.3(–12)	NA
MUPE	195	39	46	87	
LAPE	192	37	88	1,270	

[a] $2.1(-17) \equiv 2.1 \times 10^{-17}$

[b] NA denotes not available

Table 4 Calculated ($k^{CVT/SCT}$) and experimental rate constants (in cm^3 $molecule^{-1}$ s^{-1}) determined on various B1B95– *X*/6–31+G(d,p) surfaces as well as the average errors

Temperature (K)	B1B95– *X*/6–31+G(d,p)				Experimental
	$X = 32.1$	$X = 34.8$	$X = 37.0$	$X = 42.0$	
200	1.6(–17)[a]	4.0(–18)	1.2(–18)	9.1(–20)	NA[b]
250	1.5(–16)	4.6(–17)	1.6(–17)	2.0(–18)	7.0(–17)
298	6.9(–16)	2.4(–16)	1.0(–16)	1.7(–17)	2.7(–16)
300	7.3(–16)	2.6(–16)	1.1(–16)	1.8(–17)	2.9(–16)
350	2.4(–15)	9.6(–16)	4.5(–16)	9.4(–17)	8.7(–16)
400	6.2(–15)	2.7(–15)	1.4(–15)	3.4(–16)	2.1(–15)
450	1.3(–14)	6.3(–15)	3.4(–15)	9.7(–16)	4.7(–15)
500	2.5(–14)	1.3(–14)	7.3(–15)	2.3(–15)	1.1(–14)
600	7.0(–14)	3.9(–14)	2.5(–14)	9.2(–15)	2.4(–14)
700	1.6(–13)	9.3(–14)	6.2(–14)	2.6(–14)	4.1(–14)
800	3.0(–13)	1.9(–13)	1.3(–13)	6.1(–14)	NA
900	5.1(–13)	3.4(–13)	2.4(–13)	1.2(–13)	NA
1,000	8.1(–13)	5.5(–13)	4.1(–13)	2.2(–13)	NA
1,200	1.7(–12)	1.3(–12)	9.7(–13)	5.6(–13)	NA
1,500	4.2(–12)	3.2(–12)	2.6(–12)	1.6(–12)	NA
MUPE	181	42	47	78	
LAPE	176	41	92	631	

[a] $1.6(-17) \equiv 1.6 \times 10^{-17}$

[b] NA denotes not available

dynamical bottleneck regions. Figures 3, 4, and 5 show Arrhenius representations of the calculated rate constants obtained using the mPW1PW91, the B1B95, and the mPW1B95 functional, respectively, with different HF contributions. In these figures, the experimental values obtained from the fit of Schmoltner et al. [6] are represented by triangles, the values obtained from the fit of Hsu and DeMore [7] are represented by circles, the values obtained from the fit of Jeong and Kaufman [5] are represented by diamonds, the values obtained from the fit of Medhurst et al. [8] are represented by squares, and the experimental values that were used in determining the accuracy of HDFT methods, as described below, are represented by ×. Finally, Fig. 6 shows the LAPE and

Table 5 Calculated ($k^{CVT/SCT}$) and experimental rate constants (in cm^3 $molecule^{-1}$ s^{-1}) determined on various mPW1B95– *X*/6–31+G(d,p) surfaces as well as the average errors

Temperature (K)	mPW1B95– *X*/6–31+G(d,p)				Experimental
	$X = 35.4$	$X = 38.5$	$X = 41.0$	$X = 44.0$	
200	2.4(–17)[a]	4.4(–18)	1.2(–18)	2.4(–19)	NA[b]
250	2.0(–16)	4.7(–17)	1.6(–17)	4.2(–18)	7.0(–17)
298	8.4(–16)	2.5(–16)	9.4(–17)	3.1(–17)	2.7(–16)
300	8.8(–16)	2.6(–16)	1.0(–16)	3.3(–17)	2.9(–16)
350	2.8(–15)	9.5(–16)	4.1(–16)	1.6(–16)	8.7(–16)
400	6.9(–15)	2.6(–15)	1.3(–15)	5.3(–16)	2.1(–15)
450	1.4(–14)	6.1(–15)	3.1(–15)	1.4(–15)	4.7(–15)
500	2.7(–14)	1.2(–14)	6.7(–15)	3.3(–15)	1.1(–14)
600	7.3(–14)	3.7(–14)	2.2(–14)	1.2(–14)	2.4(–14)
700	1.6(–13)	8.9(–14)	5.7(–14)	3.4(–14)	4.1(–14)
800	3.0(–13)	1.8(–13)	1.2(–13)	7.5(–14)	NA
900	5.1(–13)	3.2(–13)	2.2(–13)	1.5(–13)	NA
1,000	8.1(–13)	5.3(–13)	3.8(–13)	2.6(–13)	NA
1,200	1.7(–12)	1.2(–12)	8.9(–13)	6.4(–13)	NA
1,500	4.1(–12)	3.0(–12)	2.4(–12)	1.8(–12)	NA
MUPE	216	38	49	69	
LAPE	212	37	104	353	

[a] $2.4(-17) \equiv 2.4 \times 10^{-17}$

[b] NA denotes not available

MUPE in calculated rate constants versus the percentage of HF exchange for all three types of functionals investigated in this study.

4 Analysis and discussion

4.1 Parameterized HDFT methods

The goal of this study is to determine the HDFT methods that provide accurate calculated rate constants for the title reaction using VTST/MT. For each of the three functionals investigated here, we initially carried out direct dynamics calculations using the functionals designed for kinetics (i.e., the K methods: MPW1K, BB1K, and MPWB1K, respectively). We performed a second set of dynamics calculations using the three HDFT methods (mPW1PW91—35.7, B1B95—37.0, and mPW1B95—41.0) that give accurate rate constants for the HO + CH_3F reaction [42]. We carried out a third set of dynamics calculations using the three HDFT methods (mPW1PW91—30.7, B1B95—32.1, and mPW1B95—35.4) that were determined (using a linear extrapolation methodology similar to the one described in more detail elsewhere [70]) to have a classical barrier height close to the modified G2 calculated value of 5.8 kcal/mol [13].

Finally, we chose another set of HDFT methods based on the experimental rate constants at 400 K as follows. We defined a target experimental rate constant value of 2.39×10^{-15} cm^3 break $molecule^{-1}$ s^{-1} at 400 K that was obtained as an average of four rate constants (1.78×10^{-15}, 2.09×10^{-15}, 2.21×10^{-15}, and 3.50×10^{-15} cm^3 $molecule^{-1}$ s^{-1}, respectively) obtained from the four available experimental fits [5–8]. The temperature of 400 K was chosen because this value is in or close to the temperature range for the fits available [5–8]. (The value of the experimental rate constant at 400 K in Tables 3, 4, and 5 is based, however, only on the fit of Jeong and Kaufman [5].) On the basis of the preliminary results from the first two sets of dynamics calculations, assuming a linear relationship between $\log k^{CVT/SCT}$ versus the HF exchange contribution (X), we determined three new HDFT methods: mPW1PW91—33.5, B1B95—34.8, and mPW1B95—38.5. After carrying out dynamics calculations, we indeed determined that these methods provide calculated rate constants within an acceptable range (15%) of the target experimental rate constant at 400 K.

In Tables 1 and 2, we also present results obtained for the generic mPW1PW91, B1B95, and mPW1B95 methods (with $X = 25.0$, $X = 28.0$, and $X = 31.0$, respectively). These results were determined only from the properties of the saddle point; no dynamics calculations were carried out using these methods.

4.2 Calculated rate constants

On three surfaces, mPW1PW91—33.5, B1B95—34.8, and mPW1B95—38.5, we carried out dynamics calculations involving both SCT approximation and LCT

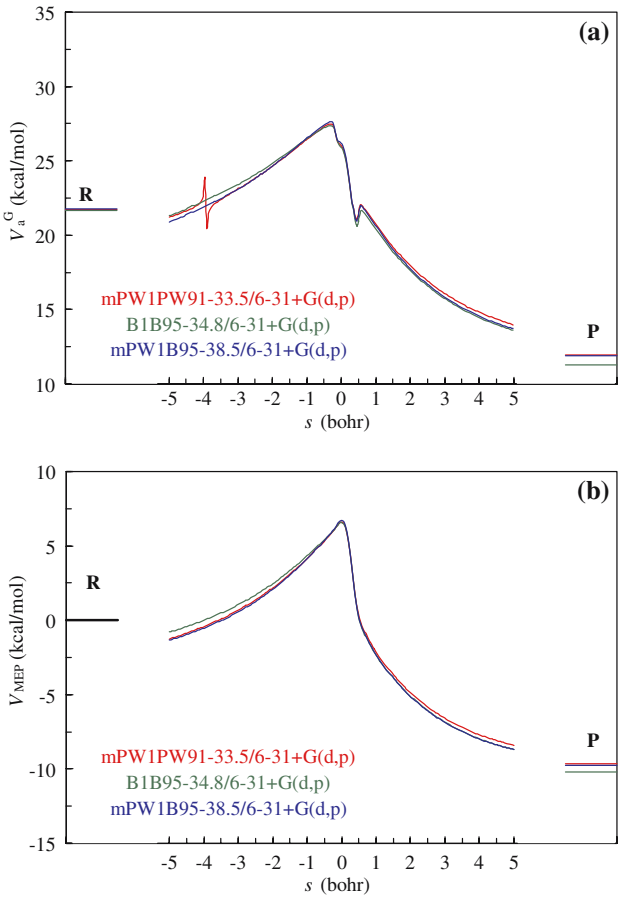

Fig. 1 Reaction path profiles ($-5.0a_0 < s < +5.0a_0$) for $OH + CHF_3 \rightarrow H_2O + CF_3$ reaction determined on three HDFT surfaces that provide accurate calculated rate constants. **a** The vibrationally adiabatic ground-state potential energy curves, V_a^G, and **b** The potential energy curves along the minimum energy path, V_{MEP}. R represents the reactant state and *P* represents the product state

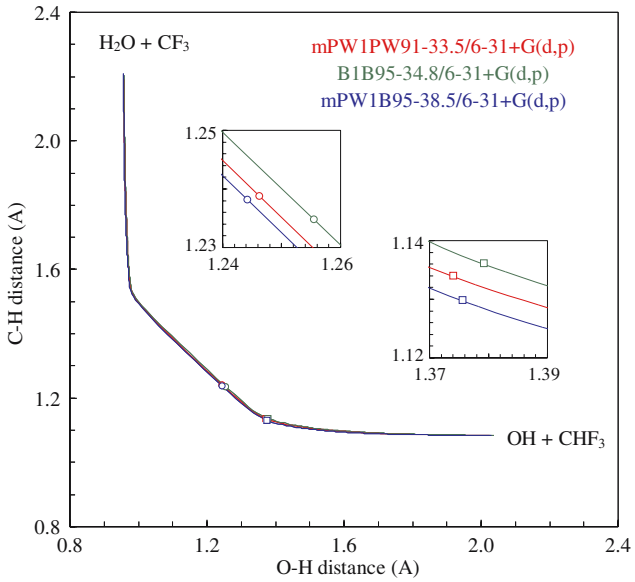

Fig. 2 A two-dimensional representation of the reaction paths ($-5.0a_0 < s < +5.0a_0$) determined on three HDFT surfaces that provide accurate calculated rate constants. The *circles* represent the saddle points, $s = 0$, the *squares* represent the dynamical bottlenecks at 298 K, $s_*^{CVT}(298)$

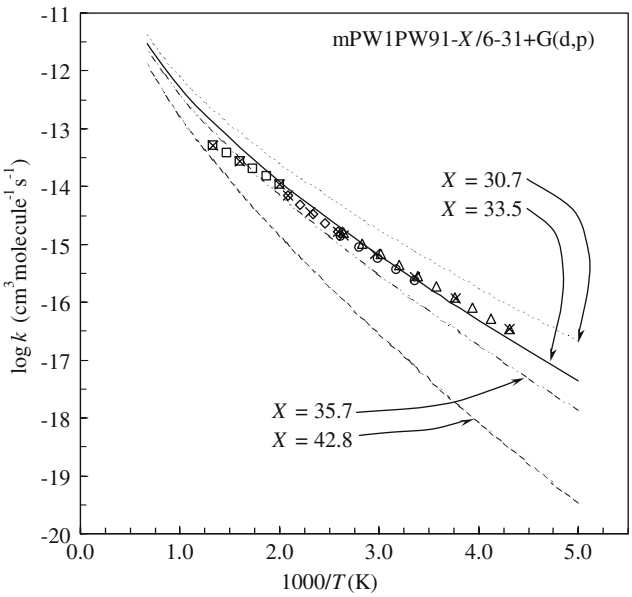

Fig. 3 Arrhenius plot of CVT/SCT rate constants calculated on mPW1PW91–*X*/6–31+G(d,p) surfaces compared with experimental results

approximation to account for quantum mechanical effects along the reaction coordinate. On all these surfaces, the title reaction is dominated by small-curvature tunneling. In particular, the SCT rate constants ($k^{CVT/SCT}$) are always larger than the LCT rate constants ($k^{CVT/LCT}$). Moreover, within 2% or less, $k^{CVT/\mu OMT}$ is well approximated by $k^{CVT/SCT}$. Similar results were obtained for the hydrogen abstraction reaction from fluoromethane by hydroxyl radical [42]. We therefore carried out the dynamics calculations on the other PESs using only SCT approximation for tunneling contributions. Because we checked that $k^{CVT/SCT}$ is always greater than $k^{CVT/LCT}$, the CVT/SCT results could be relabeled CVT/COMT, if desired, since they are canonically optimized.

The CVT/SCT rate constants calculated on all investigated HDFT surfaces over the temperature range 200–1500 K are given in Tables 3, 4, and 5. The errors are also given in these tables, but they are calculated over the smaller temperature range, where experimental data is available, as described subsequently. There are four available experimental data fits (given by Eqs. 2–5) over temperature intervals such that all of them cover the 232–750 K temperature range. The analysis of the accuracy of an HDFT method was carried out using a set

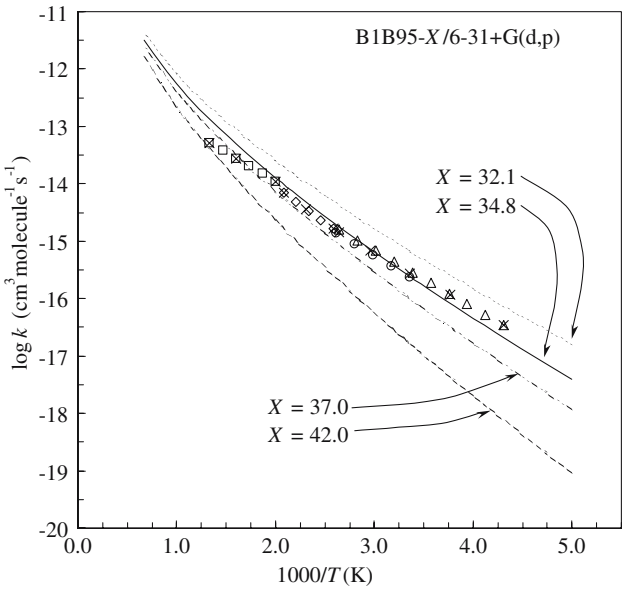

Fig. 4 Arrhenius plot of CVT/SCT rate constants calculated on B1B95– *X*/6–31+G(d,p) surfaces compared with experimental results

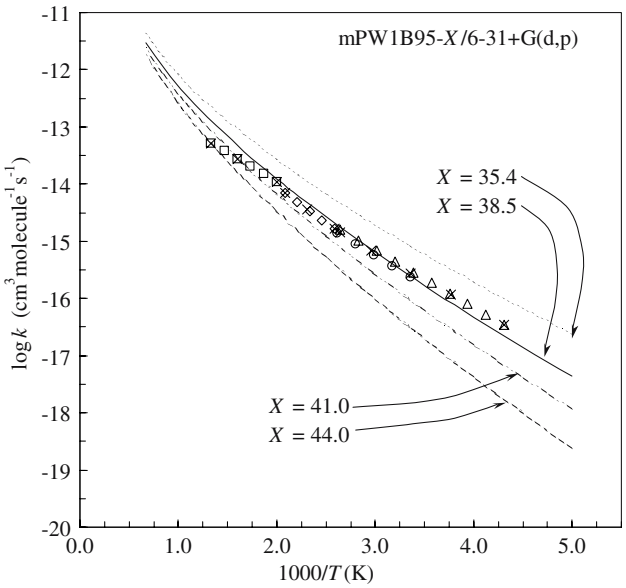

Fig. 5 Arrhenius plot of CVT/SCT rate constants calculated on mPW1B95– *X*/6–31+G(d,p) surfaces compared with experimental results

of 11 temperatures. These 11 temperatures are seven end points of the four experimental fits (232, 298, 378, 387, 480, 500, and 750 K) and another four temperatures (265, 338, 433, and 625 K) that are the median of four of the six temperature intervals defined by the original seven points. (The 378 K end point of one fit and the 383 K end point of another fit were close enough that

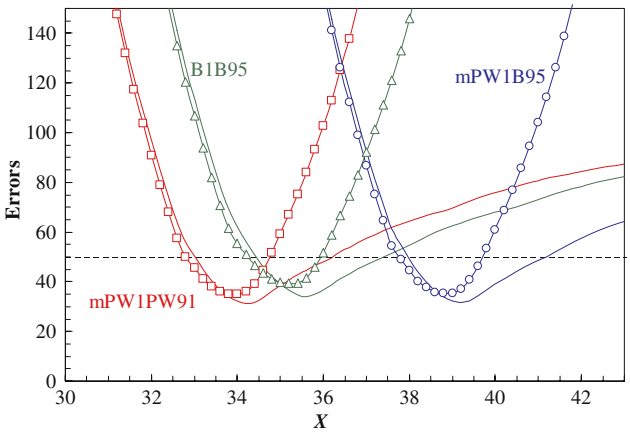

Fig. 6 Average percentage error of all the three methods as a function of the HF exchange contribution to the exchange-correlation functional. LAPE are the curves with symbols (*squares* for mPW1PW91—*X*, *triangles* for B1B95—*X*, and *circles* for mPW1B95—*X*), MUPE are the curves *without symbols*

we included only one of them, namely the 378 K.) For three of these temperatures (298, 338, and 378 K) there are two fits available, and the experimental rate constants were obtained as the average of the two values obtained from each available fit. For the other eight temperatures, only one experimental fit is available, and that fit was used to obtain the experimental rate constant at that temperature.

For each one of these 11 temperatures and for each functional, we fitted the four calculated $\log k^{\mathrm{CVT/SCT}}$ versus the HF exchange contribution (X) representation to a second order polynomial. For each functional, this fit was then used to calculate a rate constant for each value of X within a certain range. (The quadratic polynomial fits are provided as Supplementary Material.) Knowing $\log k^{\mathrm{CVT/SCT}}$ as a function of the X value, one can calculate the MUPE and LAPE as a function of the X value. The LAPE and MUPE versus X representations for all three examined functionals are given in Fig. 6. This figure illustrates the X value range that one should use to obtain calculated rate constants (using the VTST/MT dynamics calculations on a PES obtained using HDFT method in conjunction with the 6–31+G(d,p) basis set) that are, on average, within a certain desired accuracy with respect to the experimental values.

In interpreting these results (and in calculating rate constants that are not available experimentally), one would (or should) be satisfied if the average error in the calculated rate constants is less than 50%. It is of course preferred to obtain errors much smaller than this, but one should take into account that direct dynamics results using the VTST/MT give rate constants that are, on average, within 25–30% of the experimental or

the accurate quantum mechanical dynamics rate constants [55,71,72]. Our dynamics calculations also include additional approximations (such as not including the anharmonicity or not using scaled vibrational frequencies in calculating vibrational partition functions) that may increase (although they can also decrease) the inaccuracy of the calculated rate constants, so accepting 50% errors in calculated rate constants is reasonable. (For kinetic isotope effects calculations, the errors would be, however, larger than 50% if the rate constants for isotopic substituted reactants were on opposite directions of the experimental values.) Our analysis gives the range of X that provides calculated rate constants that are within 50% of the experimental data. These are 32.8–34.8 using mPW1PW91, 34.2–36.0 using B1B95, and 37.8–39.7 using mPW1B95 functionals, respectively. The optimal values of X are 33.9 for mPW1PW91, 35.3 for B1B95, and 38.9 for mPW1B95 functionals, respectively. The lowest LAPE obtained with either one of these HDFT methods (with optimal X values) is around 35%. In comparison, for the HO+CH_3F reaction we obtained average errors as low as 5% [42]. The higher average errors obtained here for the HO + CHF_3 reaction is due to the fact that no PES employed here accurately reproduces the experimental rate constants both at very low temperatures and at high temperatures. From Figs. 3, 4, and 5, it is noticeable that the HDFT methods with higher X reproduce better the experimental results at higher temperatures (than at lower temperatures), while the HDFT methods with lower X reproduce better the experimental results at lower temperatures (than at higher temperatures). It is also interesting to point out that among the K methods, similar to the results for the HO + CH_3F reaction [42], mPWB1K give better results (LAPE = 353) than BB1K (LAPE = 631), which in turn is better than MPW1K (LAPE = 1,270).

Our direct dynamics calculations show that the tunneling contributions for this reaction can be significant at very low temperatures. At 298 K, among the three HDFT methods that give accurate rate constants, the transmission coefficient is the highest for the mPW1B95 −38.5 functional ($\kappa^{SCT} = 2.46$), then the mPW1PW91 −33.5 functional ($\kappa^{SCT} = 2.27$), and the smallest for the B1B95−34.8 functional ($\kappa^{SCT} = 2.02$). The tunneling contributions are even more significant at lower temperatures. Although the multidimensional tunneling calculations employed here involve information along the whole reaction path, the results are consistent with one's expectation based on the saddle point properties. The tunneling is expected to be more significant on the PES with a higher classical barrier height and a higher imaginary frequency at the saddle point, and we indeed observe this trend. Tunneling is also more significant on the PES with a smaller perpendicular looseness, a quantity that will be defined in Sect. 4

As discussed in more detail in the study of the HO + CH_3F reaction [42], the use of scaled vibrational frequencies or the inclusion of anharmonicity effects will increase the calculated rate constants leading to a slightly lower optimal value of the HF exchange contribution. The differences were however found to be within our reliability range of 50%, and we expect the same behavior for the title reaction.

One possible use of the present kind of study is predicting the rate constant outside the range where it has been measured. For example, the three SRP potentials presented here predict k at 200 K to be in the range 4.0–4.5 $\times 10^{-18}$ cm^3 $molecule^{-1}$ s^{-1}, but since the rates are underestimated at 250–300 K, this would be a predicted lower bound; and k at 1,500 K is predicted to be in the range 3.0–3.2 $\times 10^{-12}$ cm^3 $molecule^{-1}$ s^{-1} but since the rates are overestimated at 350–700 K, this should be interpreted as an approximate upper bound.

4.3 Reaction energetics

One of the advantages of using HDFT methods in creating PES for dynamics calculations is that the energetics in the saddle point region is very dependent on the HF exchange contribution. Inspecting the results in Table 1, one obvious observation is that the calculated classical barrier height increases with the increase in the HF exchange contribution to the exchange-correlation energy. The generic HDFT methods (with lower values of X) give small barrier heights, and the HDFT methods designed for kinetics (i.e., the K methods) apparently slightly overestimate the classical barrier height, with calculated values of 9.3, 8.6, and 8.3 kcal/mol for MPW1K, BB1K, and MPWB1K, respectively. The HF exchange contribution that one uses to get a certain barrier height depends on the choice of gradient-corrected exchange and correlation functional used. To obtain a barrier height of a certain value, one should use higher HF exchange contribution for mPW1B95 functional than for the B1B95 functional or the mPW1PW91 functional. For example, the mPW1PW91−30.7, B1B95−32.1, and mPW1B95−35.4 methods give classical barrier heights of 5.79, 5.79, and 5.81 kcal/mol, respectively (i.e., the same barrier height) by using different (i.e., increasing) HF exchange contributions.

To find the value of the classical barrier height, we investigate in more detail the HDFT surfaces that give accurate rate constants in conjunction with the VTST/MT dynamics calculations. To be more precise, one should find a range of X values and a range of barrier height values that provide accurate results. For each

of the three functionals investigated, we fitted the calculated barrier heights versus X to a quadratic form and found, on the basis of the fit and knowing the limits of X that give calculated rate constants within the acceptable accuracy range of 50%, classical barrier heights of 6.41–7.00 kcal/mol for the mPW1PW91 functional, 6.40–6.91 kcal/mol for the B1B95 functional, and 6.53–7.09 kcal/mol for the mPW1B95 functional. Combining the results for all three functionals examined here, we propose a best estimate range of 6.5–6.9 kcal/mol for the title reaction. (The most accurate rate constants are obtained for surfaces with an average classical barrier height of 6.77 kcal/mol.) This classical barrier height estimate is significantly higher than the modified G2 [24] value of 5.8 kcal/mol determined by Korchowiec et al. [13].

The calculated enthalpy of reaction on all the HDFT surfaces, given in Table 1, is slightly less negative than the experimental value of -12.6 ± 0.7 kcal/mol at 0 K. The discrepancy increases as the HF exchange contribution increases. Based on the experimental value of the enthalpy of reaction and our calculated classical barrier height value of 6.8 kcal/mol for the forward reaction, we can predict a classical barrier height for the reverse reaction of 19.4 kcal/mol. This value is higher than the HDFT–SRP calculated values by approximately 2.5 kcal/mol.

4.4 Saddle point and dynamical bottleneck properties

The results in Table 2 show that the HDFT methods with smaller X values give early transition states characterized by shorter C···H distances and longer H···O distances, whereas the HDFT methods with bigger X values give late (or later) transition states. We also investigated the sum of the making ($r^{\ddagger}_{\mathrm{H\cdots O}}$) and breaking ($r^{\ddagger}_{\mathrm{C\cdots H}}$) bond distances. This sum, called perpendicular looseness, is a measure of the looseness of the structure in a direction perpendicular to the reaction coordinate. We found that the transition state gets looser as the HF exchange contribution decreases. When only the three HDFT methods that give accurate calculated rate constants are compared, the mPW1B95—38.5 method gives a slightly tighter transition state ($r^{\ddagger}_{\mathrm{C\cdots H}} + r^{\ddagger}_{\mathrm{H\cdots O}} = 2.482$ A) while B1B95—34.8 method gives a slightly looser transition state ($r^{\ddagger}_{\mathrm{C\cdots H}} + r^{\ddagger}_{\mathrm{H\cdots O}} = 2.490$ A). This is also seen in Fig. 2 where the reactions paths and the saddle point locations (in inset) are represented. The difference is mainly due to a longer H···O distance at the transition state. Note also that the C···H···O angle is less than 180° so $r^{\ddagger}_{\mathrm{C\cdots O}} < r^{\ddagger}_{\mathrm{C\cdots H}} + r^{\ddagger}_{\mathrm{H\cdots O}}$. For the HDFT methods used in this study and the 6–31+G(d,p) basis set, the C···H···O angle is around 172°.

The imaginary frequency at the saddle point can be seen as a measure of the thickness of the barrier. A high imaginary frequency indicates a large negative force constant for the reaction coordinate mode at the saddle point and, therefore, at least near the barrier top, a thin barrier. All other factors being equal, a thinner barrier gives increased tunneling probabilities in dynamics calculations. Among the HDFT methods that give the same (or very similar) rate constants, the mPW1B95 functional gives the narrowest barrier (highest value for the imaginary frequency and the smallest perpendicular looseness) and the B1B95 functional gives the widest barrier. Not surprising, the calculated transmission coefficients are calculated to be higher for the mPW1B95 functional. Based on our results, the best estimate of the imaginary frequency at the saddle point is $1{,}530i\,\mathrm{cm}^{-1}$.

The dynamical bottleneck at 298 K is located at $s = 0.286\ a_0, s = 0.287\ a_0$, and $s = 0.290\ a_0$ using mPW1PW91—33.5, B1B95—34.8, and mPW1B95—38.5 method, respectively. At the dynamical bottleneck, the C···H distance is around 1.133 A, and the O···H distance is around 1.376 A (Fig. 2 inset). The location of the dynamical bottleneck, quite far away from the saddle point, illustrates large variational effects for this reaction. This leads also to significant differences between the calculated k^{CVT} and k^{TST} (see the rate constants given as Supplementary Material).

5 Summary and concluding remarks

The HDFT methods are quite flexible in the choice of exchange and correlation functional that one uses, and this property makes them very attractive methods for use in chemical dynamics studies. Our interest is in obtaining the HDFT methods that can be used for accurately investigating chemical dynamics of important environmental and atmospheric processes.

In this work, we have developed potential energy surfaces for the $OH + CHF_3 \rightarrow H_2O + CF_3$ reaction based on hybrid density functional theory methods with a specific reaction parameter. These new HDFT methods, in conjunction with the 6–31+G(d,p) basis set, are used in calculating dynamic properties on single-level, accurate PESs without the use of dual-level dynamics. We carried out direct dynamics calculations on these surfaces using variational transition state theory with multidimensional tunneling contributions between 200 and 1,500 K. We determined three HDFT surfaces that give dynamics results that are in excellent agreement with available experimental data. The specific-reaction-parameter surfaces that give accurate calculated rate constants have an

average classical barrier height of 6.77 kcal/mol, which is our best estimate for this reaction, although, since our temperature dependence is consistently higher than the experimental one, our barrier height might be too high as well.

The optimal HF exchange contributions obtained in this study are just slightly different than the values obtained for the $OH + CH_3F \rightarrow H_2O + CH_2F$ reaction [42]. To determine if the methods developed here are transferable to other hydrogen abstraction processes, we are currently investigating, using the same approach, the hydrogen abstraction reactions from difluoromethane [73] and fluoroethanes [74]. Preliminary results show that the HDFT–SRP surfaces are appropriate for accurate direct dynamics studies of hydrogen abstraction reactions from more complex hydrofluorocarbons for which less (or no) experimental data is available.

The keywords to carry out mPW1PW91—33.5 calculations in Gaussian03 are mPWPW91/6–31+G(d,p) and IOP(3/76 = 0665003350). The keywords to carry out B1B95—34.8 calculations in Gaussian03 are BB95/6–31+G(d,p) and IOP(3/76 = 0652003480). The keywords to carry out mPW1B95—38.5 calculations in Gaussian03 are mPWB95/6–31+G(d,p) and IOP(3/76 = 0615003850).

Acknowledgments This research was supported in part by the Tennessee Technological University through a Faculty Research Initiation Program.

References

1. Brasseur GP, Orlando JJ, Tyndall GS (1999) Atmospheric chemistry and global change. Oxford University Press, New York
2. Elkins JW(1999) In: Alexander DE, Fairbridge, RW (eds) Encyclopedia of environmental science. Kluwer, Boston, p 78
3. Howard CJ, Evenson KM (1976) J Chem Phys 64:197
4. Nip WS, Singleton DL, Overend R, Paraskevopoulos G (1979) J Phys Chem 83:2440
5. Jeong KM, Kaufman F (1982) J Phys Chem 86:1808
6. Schmoltner AM, Talukdar RK, Warren RF, Mellouki A, Goldfarb L, Gierczak T, McKeen SA, Ravishankara AR (1993) J Phys Chem 97:8976
7. Hsu KJ, DeMore WB (1995) J Phys Chem 99:1235
8. Medhurst LJ, Fleming J, Nelson HH (1997) Chem Phys Lett 266:607
9. Jeong KM, Kaufman F (1982) J Phys Chem 86:1816
10. Cohen N, Benson SW (1987) J Phys Chem 91:162
11. Fu Y, Lewis-Bevan W, Tyrrell J (1995) J Phys Chem 99:630
12. Schwartz M, Marshall P, Berry RJ, Ehlers CJ, Petersson GA (1998) J Phys Chem A 102:10074
13. Korchowiec J, Kawahara S-i, Matsumura K, Uchimaru T, Sugie M (1999) J Phys Chem A 103:3548
14. Louis F, Gonzalez CA, Huie RE, Kurylo MJ (2000) J Phys Chem A 104:8773
15. El-Taher S (2001) Int J Quantum Chem 84:426
16. Korchowiec J (2002) J Phys Org Chem 15:524
17. M⊘ller C, Plesset MS (1934) Phys Rev 46:618
18. Schlegel HB (1986) J Chem Phys 84:4530
19. Sosa C, Schlegel HB (1986) Int J Quantum Chem 29:1001
20. Schlegel HB (1988) J Phys Chem 92:3075
21. Wigner E (1932) Z Phys Chem B 19:203
22. Curtiss LA, Raghavachari K, Trucks GW, Pople JA (1991) J Chem Phys 94:7221
23. Curtiss LA, Raghavachari K, Pople JA (1993) J Chem Phys 98:1293
24. Mebel AM, Morokuma K, Lin MC (1995) J Chem Phys 103:7414
25. Garrett BC, Truhlar DG (1979) J Phys Chem 83:2921
26. Garrett BC, Truhlar DG (1979) J Chem Phys 70:1593
27. Truhlar DG, Garrett BC (1980) Acc Chem Res 13:440
28. Garrett BC, Truhlar DG (1984) J Chem Phys 81:309
29. Truhlar DG, Garrett BC (1984) Ann Rev Phys Chem 35:159
30. Truhlar DG, Garrett BC, Hipes PG, Kuppermann A (1984) J Chem Phys 81:3542
31. Truhlar DG, Isaacson AD, Garrett BC (1985) In: Baer M (ed) Theory of chemical reaction dynamics, vol 4. CRC Press, Boca Raton, pp 65
32. Kreevoy MM, Truhlar DG (1986) In: Bernasconi CF (ed) Investigation of rates and mechanisms of reactions, vol 6. Wiley, New York, pp 13
33. Tucker SC, Truhlar DG (1989) In: Bertran J IGC (ed) New theoretical concepts understanding organic reactions, vol 267. Kluwer, Dordrecht, pp 291
34. Liu YP, Lynch GC, Truong TN, Lu DH, Truhlar DG, Garrett BC (1993) J Am Chem Soc 115:2408
35. Truhlar DG, Garrett BC, Klippenstein SJ (1996) J Phys Chem 100:12771
36. Garrett BC, Truhlar DG (2005) In: Dykstra CE, Frenking, G, Kim, K, Scuseria, G (eds) Theory and applications of computational chemistry: the first forty years. Elsevier, Amsterdam, pp 67
37. Coote ML (2004) J Phys Chem A 108:3865
38. Zhao Y, Truhlar DG (2004) J Phys Chem A 108:6908
39. Andersson S, Gruening M (2004) J Phys Chem A 108:7621
40. Zhao Y, Truhlar DG (2005) J Phys Chem A 109:5656
41. Gonzalez-Lafont A, Truong TN, Truhlar DG (1991) J Phys Chem 95:4618
42. Albu TV, Swaminathan S (2006) J Phys Chem A 110:7663
43. Pu J, Truhlar DG (2002) J Chem Phys 116:1468
44. Hu WP, Liu YP, Truhlar DG (1994) J Chem Soc Faraday Trans 90:1715
45. Corchado JC, Coitino EL, Chuang Y-Y, Fast PL, Truhlar DG (1998) J Phys Chem A 102:2424
46. Chuang Y-Y, Corchado JC, Truhlar DG (1999) J Phys Chem A 103:1140
47. Albu TV, Corchado JC, Truhlar DG (2001) J Phys Chem A 105:8465
48. Truhlar DG, Kuppermann A (1971) J Am Chem Soc 93:1840
49. Bell RL, Truong TN (1994) J Chem Phys 101:10442
50. Garrett BC, Truhlar DG (1979) J Phys Chem 83:1915
51. Lin H, Zhao Y, Ellingson BA, Pu J, Truhlar DG (2005) J Am Chem Soc 127:2830
52. Lu D-h, Truong TN, Melissas VS, Lynch GC, Liu Y-P, Garrett BC, Steckler R, Isaacson AD, Rai SN, Hancock GC, Lauderdale JG, Joseph T, Truhlar DG (1992) Comput Phys Commun 71:235
53. Liu YP, Lu DH, Gonzalez-Lafont A, Truhlar DG, Garrett BC (1993) J Am Chem Soc 115:7806
54. Truong TN, Lu D-h, Lynch GC, Liu Y-P, Melissas VS, Steward JJP, Steckler R, Garrett BC, Isaacson AD, Gonzalez-Lafont A, Rai SN, Hancock GC, Joseph T, Truhlar DG (1993) Comput Phys Commun 75:143

55. Allison TC, Truhlar DG (1998) In: Thompson DL (ed) Modern methods for multidimensional dynamics computations in chemistry. World Scientific, Singapore, pp 618
56. Fernandez-Ramos A, Truhlar DG (2001) J Chem Phys 114:1491
57. Perdew JP, Chevary JA, Vosko SH, Jackson KA, Pederson MR, Singh DJ, Fiolhais C (1992) Phys Rev B 46:6671
58. Adamo C, Barone V (1998) J Chem Phys 108:664
59. Lynch BJ, Fast PL, Harris M, Truhlar DG (2000) J Phys Chem A 104:4811
60. Becke AD (1988) Phys Rev A 38:3098
61. Becke AD (1993) J Chem Phys 98:5648
62. Becke AD (1996) J Chem Phys 104:1040
63. Zhao Y, Lynch BJ, Truhlar DG (2004) J Phys Chem A 108:2715
64. Gaussian 03, Revision B.02, Frisch MJ, Trucks GW, Schlegel HB, Scuseria GE, Robb MA, Cheeseman JR, Montgomery J, J. A.;, Vreven T, Kudin KN, Burant JC, Millam JM, Iyengar SS, Tomasi J, Barone V, Mennucci B, Cossi M, Scalmani G, Rega N, Petersson GA, Nakatsuji H, Hada M, Ehara M, Toyota K, Fukuda R, Hasegawa J, Ishida M, Nakajima T, Honda Y, Kitao O, Nakai H, Klene M, Li X, Knox JE, Hratchian HP, Cross JB, Adamo C, Jaramillo J, Gomperts R, Stratmann RE, Yazyev O, Austin AJ, Cammi R, Pomelli C, Ochterski JW, Ayala PY, Morokuma K, Voth GA, Salvador P, Dannenberg JJ, Zakrzewski VG, Dapprich S, Daniels AD, Strain MC, Farkas O, Malick DK, Rabuck AD, Raghavachari K, Foresman JB, Ortiz JV, Cui Q, Baboul AG, Clifford S, Cioslowski J, Stefanov BB, Liu G, Liashenko A, Piskorz P, Komaromi I, Martin RL, Fox DJ, Keith T, Al-Laham MA, Peng CY, Nanayakkara A, Challacombe M, Gill PMW, Johnson B, Chen W, Wong MW, Gonzalez C, Pople JA (2003) Gaussian Inc., Pittsburgh
65. GAUSSRATE 9.1 Corchado JC, Chuang Y-Y, Coitiño EL, Truhlar DG (2003)University of Minnesota, Minneapolis
66. POLYRATE 9.1, Corchado JC, Chuang Y-Y, Fast PL, Villà J, Hu W-P, Liu Y-P, Lynch GC, Nguyen KA, Jackels CF, Melissas VS, Lynch BJ, Rossi I, Coitiño EL, Fernandez-Ramos A, Pu J, Albu TV, Steckler R, Garrett BC, Isaacson AD, Truhlar DG (2003) University of Minnesota, Minneapolis
67. Page M, McIver JW, Jr (1988) J Chem Phys 88:922
68. Chuang Y-Y, Truhlar DG (1998) J Phys Chem A 102:242
69. The vibrationally adiabatic ground-state potential energy curves obtained on mPW1PW91–33.5 surface has an unphysical bump on the reactant side that is due to numerical errors in the calculation of the generalized normal modes. This result does not however change at all the calculated rate constants.
70. Mikel SE, Albu TV (2006) J Und Chem Res 5:75
71. Pu J, Corchado JC, Truhlar DG (2001) J Chem Phys 115:6266
72. Pu J, Truhlar DG (2002) J Chem Phys 117:1479
73. Albu TV, Swaminathan S (manuscript in preparation)
74. Albu TV, De Silva NWSVN (manuscript in preparation)